

Tuning-free multi-coil compressed sensing MRI with Parallel Variable Density Approximate Message Passing (P-VDAMP)

Charles Millard¹, Mark Chiew¹, Jared Tanner², Aaron T. Hess¹ and Boris Mailhé³

¹ Wellcome Centre for Integrative Neuroimaging, FMRIB, Nuffield Department of Clinical
Neurosciences, University of Oxford, Oxford, UK

² Mathematical Institute, University of Oxford, Oxford, UK

³ Siemens Healthineers, Princeton, NJ, USA

Corresponding author: Charles Millard, Wellcome Centre for Integrative Neuroimaging,
FMRIB, Nuffield Department of Clinical Neurosciences, University of Oxford, Level 0, John
Radcliffe Hospital, Oxford, OX3 9DU, UK. email: charles.millard@exeter.ox.ac.uk

Word count: 4998

Running title: Tuning-free multi-coil compressed sensing MRI with P-VDAMP

Key words: Compressed sensing, Parallel Imaging, Approximate Message Passing, Stein's
Unbiased Risk Estimate (SURE)

Submitted to Magnetic Resonance in Medicine on 8th March 2022

Abstract

Purpose: To develop a tuning-free method for multi-coil compressed sensing MRI that performs competitively with algorithms with an optimally tuned sparse parameter.

Theory: The Parallel Variable Density Approximate Message Passing (P-VDAMP) algorithm is proposed. For Bernoulli random variable density sampling, P-VDAMP obeys a “state evolution”, where the intermediate per-iteration image estimate is distributed according to the ground truth corrupted by a Gaussian vector with approximately known covariance. State evolution is leveraged to automatically tune sparse parameters on-the-fly with Stein’s Unbiased Risk Estimate (SURE).

Methods: P-VDAMP is evaluated on brain, knee and angiogram datasets at acceleration factors 5 and 10 and compared with four variants of the Fast Iterative Shrinkage-Thresholding algorithm (FISTA), including two tuning-free variants from the literature.

Results: The proposed method is found to have a similar reconstruction quality and time to convergence as FISTA with an optimally tuned sparse weighting.

Conclusions: P-VDAMP is an efficient, robust and principled method for on-the-fly parameter tuning that is competitive with optimally tuned FISTA and offers substantial robustness and reconstruction quality improvements over competing tuning-free methods.

Introduction

Reducing acquisition time is one of the main challenges for rapid, dynamic MRI. Accordingly, there is considerable research attention on techniques that reconstruct sub-sampled k-space data without substantially sacrificing image quality. Parallel imaging exploits the non-uniformity of coil sensitivities to reconstruct data that have been simultaneously acquired over a multichannel array of receiver coils^{1,2,3,4}. More recently, compressed sensing^{5,6} has been applied to MRI to accommodate further acceleration^{7,8,9}, using presumed redundancy in the signal and regularised optimisation techniques to reconstruct incoherently sampled data.

A frequently noted challenge for compressed sensing MRI (CS-MRI) is how to tune model parameters^{10,11,12}, which is typically done by hand¹³. The ideal parameter choice depends on a multitude of case-specific factors including the anatomy, underlying MR physics and sampling strategy, so hand-tuning generally yields sub-optimal reconstruction. For reliably high quality CS-MRI reconstruction, a robust, accurate and computationally efficient method for automatic parameter tuning is desirable.

Many existing methods for automatic parameter tuning depend on a testing procedure, where the reconstruction algorithm is run multiple times^{14,15,16,17}. In general this is a highly computationally intensive process, especially for models with multiple parameters. The focus of this paper is on algorithms that tunes model parameters on-the-fly, so that the algorithm only needs to be run once^{18,19}.

A natural candidate for automatic on-the-fly parameter tuning is Stein’s Unbiased Risk Estimate (SURE)²⁰. SURE efficiently estimates the squared error of a denoised vector, so can be used as a proxy for the actual error to tune parameters of a denoising function²¹. In CS-MRI, random sampling ensures that the aliasing is “noise-like”, suggesting that the application of SURE may be valid. However, SURE only gives near-optimal parameter selection when the noise is drawn from a zero-mean Gaussian distribution, and the per-iteration aliasing of standard CS-MRI algorithms deviates considerably from a zero-mean Gaussian in practice. Despite no guarantee that the tuning is near-optimal, there has been empirical success employing SURE for tuning-free CS-MRI^{18,22}, suggesting that SURE is somewhat robust to deviations from the appropriate noise distribution.

This paper presents a solution to the problem of aliasing model mismatch via the Approximate Message Passing (AMP) framework^{23,32,41}. The AMP algorithm was originally developed for sparse signals sampled with i.i.d. Gaussian sensing matrices²³. For such sensing matrices, it is known that AMP obeys a “state evolution”, where the intermediate signal estimate is distributed according to the reference signal corrupted by white Gaussian aliasing. State evolution ensures that SURE’s assumed aliasing distribution matches the actual aliasing, so automatic parameter tuning with SURE is truly near-optimal^{24,25,26}. However, when the sensing matrix does not satisfy its i.i.d. Gaussian assumption,

such as for CS-MRI, AMP’s state evolution may fail. The naive application of AMP to CS-MRI does not obey state evolution and does not perform well in practice. There has been a number of attempts to adapt AMP-based algorithms to CS-MRI including: Location Constrained AMP²⁸, Block-Matching 3D AMP-MRI^{29,30} Learned Denoising AMP³¹ and, for single coil measurements, Vector AMP (VAMP) for Image Reconstruction^{32,33} and Damped Denoising VAMP³⁴. Although these modifications were found to empirically improve the convergence behaviour of AMP, they do not obey state evolution so cannot be leveraged for near-optimal parameter tuning with SURE.

The authors’ recently proposed single-coil VDAMP algorithm^{35,36} is, to our knowledge, the first algorithm for Fourier sampled images that obeys a state evolution. Specifically, single-coil VDAMP obeys a “colored state evolution”, where the per-iteration aliasing is accurately characterised by one real number per wavelet subband³⁵. This paper proposes the Parallel Variable Density Approximate Message Passing (P-VDAMP) algorithm, which extends single-coil VDAMP to multiple coils. For Bernoulli sampled k-space, where sampling is random and independent, P-VDAMP’s intermediate aliasing is distributed according to a zero-mean Gaussian with a covariance matrix represented with a wavelet-domain vector with N unique entries, where N is the dimension of the reference image. We refer to this as “parallel colored state evolution”. To our knowledge, P-VDAMP is the first algorithm for multi-coil MRI that obeys a state evolution with accurately tracked parameters, and therefore the first method where parameter tuning with SURE is truly near-optimal.

Theory

Denote the N -dimensional data on coil c as

$$\mathbf{y}_c = \mathbf{M}_\Omega(\mathbf{F}\mathbf{S}_c\mathbf{x}_0 + \boldsymbol{\varepsilon}_c), \quad c = \{1, 2, \dots, N_c\} \quad (1)$$

where \mathbf{M}_Ω is a diagonal undersampling mask with 1 on the j th diagonal entry if $j \in \Omega$ and 0 otherwise, where Ω is a sampling set with $|\Omega| = n$ for $n < N$. The matrix \mathbf{F} is the discrete Fourier transform and \mathbf{S}_c is the diagonal sensitivity profile of coil c , which we assume have been normalised so that they satisfy $\sum_c \mathbf{S}_c^H \mathbf{S}_c = \mathbb{1}_N$, and \mathbf{x}_0 is the image of interest. The vector $\boldsymbol{\varepsilon}_c$ represents the measurement noise, which is modelled as complex Gaussian distributed with zero mean.

The mathematical results in this section assume that the entries of the sampling set Ω are generated independently with arbitrary variable density $\Pr(j \in \Omega) = p_j$, referred to as “Bernoulli sampling”. In other words, the sampling points correspond to Bernoulli distributed phase encodes with a fully sampled readout dimension in a Cartesian sampling framework, and (1) is a 2D subproblem that follows an inverse Fourier transform along the readout dimension. Despite not being specifically constructed for Poisson

disc sampling, we find empirically that P-VDAMP applied to Poisson disc sampled data performs well without modification.

The experimental work in this paper can be reproduced with MATLAB code available at <https://github.com/charlesmillard/P-VDAMP>.

Density compensated zero-filling and error propagation

In this section, we demonstrate that a Bernoulli sampled zero-filled image estimate has aliasing with a fully characterisable distribution. In other words, we show that state evolution holds at the first iteration. The mathematical tools developed in this section are preliminary to the full P-VDAMP algorithm presented later in this paper.

Consider the density compensated coil combined estimate from zero-filled data:

$$\hat{\mathbf{x}}_0 = \sum_c \mathbf{S}_c^H \mathbf{F}^H \mathbf{P}^{-1} \mathbf{y}_c, \quad (2)$$

where $\mathbf{P} = \mathbb{E}_\Omega\{\mathbf{M}_\Omega\}$ is the expected value of the random sampling mask, so that \mathbf{P} is diagonal with j th diagonal p_j . The \mathbf{P}^{-1} matrix ensures that $\hat{\mathbf{x}}_0$ is an unbiased estimate of \mathbf{x}_0 :

$$\begin{aligned} \mathbb{E}\{\hat{\mathbf{x}}_0\} &= \mathbb{E}\left\{\sum_c \mathbf{S}_c^H \mathbf{F}^H \mathbf{P}^{-1} \mathbf{M}_\Omega (\mathbf{F} \mathbf{S}_c \mathbf{x}_0 + \varepsilon_c)\right\} \\ &= \sum_c \mathbf{S}_c^H \mathbf{F}^H \mathbf{P}^{-1} \mathbf{P} \mathbf{F} \mathbf{S}_c \mathbf{x}_0 = \mathbf{x}_0, \end{aligned}$$

where $\mathbb{E}\{\mathbf{M}_\Omega\} = \mathbf{P}$ and $\mathbb{E}\{\varepsilon_c\} = \mathbf{0}$ has been used.

It is often stated that the role of random sampling in CS-MRI is to ensure that the undersampling artifacts of the zero-filled estimate are “noise-like”. A primary result of this paper is to show that when \mathbf{M}_Ω is Bernoulli random the undersampling artifacts of $\hat{\mathbf{x}}_0$ behave *exactly* as Gaussian noise: $\hat{\mathbf{x}}_0 = \mathbf{x}_0 + \mathcal{CN}(\mathbf{0}, \mathbf{\Sigma}_0^2)$, where $\mathcal{CN}(\mathbf{0}, \mathbf{\Sigma}^2)$ denotes the complex Gaussian distribution with zero mean and independent real and imaginary parts with covariance matrix $\mathbf{\Sigma}^2/2$. Moreover, we show that the covariance matrix $\mathbf{\Sigma}_0^2$ can be accurately and efficiently estimated with an N -dimensional vector, which we denote as $\boldsymbol{\tau}_0$.

Image-domain aliasing is colored by the non-uniform spectral density of the image and the variable density sampling scheme³⁸, so has a covariance matrix with strong off-diagonals. We employ an orthogonal wavelet transform to approximately decorrelate the aliasing, so that $\tilde{\mathbf{\Sigma}}_0^2$ is modelled as diagonal in the wavelet domain³⁵. Wavelets are commonly used in CS-MRI for sparsely representing an image, however, we emphasise that wavelets are used here as *a tool for modelling the aliasing*, and that P-VDAMP is not constrained to wavelet-domain regularisation. The competitive performance of more sophisticated image

models, including via neural networks, has been demonstrated for single-coil VDAMP³⁹, although is not the focus of this paper.

The appendix derives an approximation of the wavelet-domain covariance $\boldsymbol{\tau}_0 \approx \text{diag}(\boldsymbol{\Psi} \tilde{\boldsymbol{\Sigma}}_0^2 \boldsymbol{\Psi}^H)$, where $\boldsymbol{\Psi}$ is an orthogonal wavelet transform. The j th entry is

$$\tau_{0,j} = \boldsymbol{\xi}_j^H \left(\sum_i |\hat{\Psi}_{ji}|^2 \left[\left(\frac{1-p_i}{p_i} \right) \mathbf{y}_i \mathbf{y}_i^H + \boldsymbol{\Sigma}_{\varepsilon,i}^2 \right] \frac{m_i}{p_i} \right) \boldsymbol{\xi}_j. \quad (3)$$

Here, $\hat{\boldsymbol{\Psi}} = \boldsymbol{\Psi} \mathbf{F}^H$, p_i and m_i are the i th diagonal of \mathbf{P} and \mathbf{M}_Ω respectively, and $\boldsymbol{\Sigma}_{\varepsilon,i}^2 = \mathbb{E}\{\boldsymbol{\varepsilon}_i \boldsymbol{\varepsilon}_i^H\}$. The vectors $\boldsymbol{\xi}_j$, \mathbf{y}_i and $\boldsymbol{\varepsilon}_i$ have dimensionality N_c ; for instance, \mathbf{y}_i is the vector of k-space location i across all coils. The notation $|\cdot|^2$ refers to the entry-wise magnitude squared. As described in the appendix, the vector $\boldsymbol{\xi}_j$ approximates the coil-weighted spectral densities $\hat{\boldsymbol{\Psi}}^c = \boldsymbol{\Psi} \mathbf{S}_c^H \mathbf{F}^H$ with $\hat{\boldsymbol{\Psi}}_{ji}^c \approx \xi_{c,j} \hat{\Psi}_{ji}$. We suggest using $\xi_{c,j} = \langle |\boldsymbol{\Psi}_j|^2, \text{Diag}(\mathbf{S}_c) \rangle$, where $\boldsymbol{\Psi}_j$ is the j th row of $\boldsymbol{\Psi}$.

A visualisation of the error propagation formula is shown in Fig. 1 for a 256×256 brain dataset, which shows that $\hat{\mathbf{x}}_0 \approx \mathbf{x}_0 + \mathcal{CN}(\mathbf{0}, \boldsymbol{\Psi} \text{Diag}(\boldsymbol{\tau}_0) \boldsymbol{\Psi}^H)$ is an accurate model. The P-VDAMP algorithm presented in this paper has such aliasing not only for the zero-filled initial estimate $\hat{\mathbf{x}}_0$ but also for all further iterations $\hat{\mathbf{x}}_k$:

$$\hat{\mathbf{x}}_k \approx \mathbf{x}_0 + \mathcal{CN}(\mathbf{0}, \boldsymbol{\Sigma}_k^2), \quad (4)$$

where $\boldsymbol{\Sigma}_k^2 \approx \boldsymbol{\Psi} \text{Diag}(\boldsymbol{\tau}_k) \boldsymbol{\Psi}^H$ and $\boldsymbol{\tau}_k$ is estimated with an error propagation formula based on (3). Eqn. (4) is referred to as P-VDAMP’s “state evolution” because the “state” at every iteration can be fully characterized by $\boldsymbol{\Sigma}_k^2$.²³

Automatic parameter tuning with SURE

This section details how P-VDAMP’s state evolution can be leveraged by applying SURE²⁰, building on previous work on tuning-free AMP^{24,25,26}. Consider a random vector $\mathbf{r} = \mathbf{w}_0 + \mathcal{CN}(\mathbf{0}, \text{Diag}(\boldsymbol{\tau}))$, where $\boldsymbol{\tau}$ is known, and let an estimate of \mathbf{w}_0 be given by $\mathbf{f}(\mathbf{r}; \boldsymbol{\Theta})$, where $\boldsymbol{\Theta}$ is a parameter vector. Complex SURE takes the form^{20,35}

$$cSURE(\mathbf{f}(\mathbf{r}; \boldsymbol{\Theta}); \boldsymbol{\tau}) = \|\mathbf{f}(\mathbf{r}; \boldsymbol{\Theta}) - \mathbf{r}\|_2^2 + \boldsymbol{\tau}^T (2\partial(\mathbf{f}(\mathbf{r}; \boldsymbol{\Theta}))) - 1, \quad (5)$$

where

$$\partial_i(\mathbf{f}(\mathbf{r}; \boldsymbol{\Theta})) = \frac{1}{2} \left(\frac{\partial \Re[f_i(\mathbf{r}; \boldsymbol{\Theta})]}{\partial \Re[r_i]} + \frac{\partial \Im[f_i(\mathbf{r}; \boldsymbol{\Theta})]}{\partial \Im[r_i]} \right). \quad (6)$$

Here, $\Re[\cdot]$ and $\Im[\cdot]$ are the real and imaginary parts respectively. cSURE is powerful tool in practice as it is an unbiased estimate of the squared error of the denoised image,

$$\mathbb{E}\{\|\mathbf{f}(\mathbf{r}; \boldsymbol{\Theta}) - \mathbf{w}_0\|_2^2\} = \mathbb{E}\{cSURE(\mathbf{f}(\mathbf{r}; \boldsymbol{\Theta}); \boldsymbol{\tau})\} \quad (7)$$

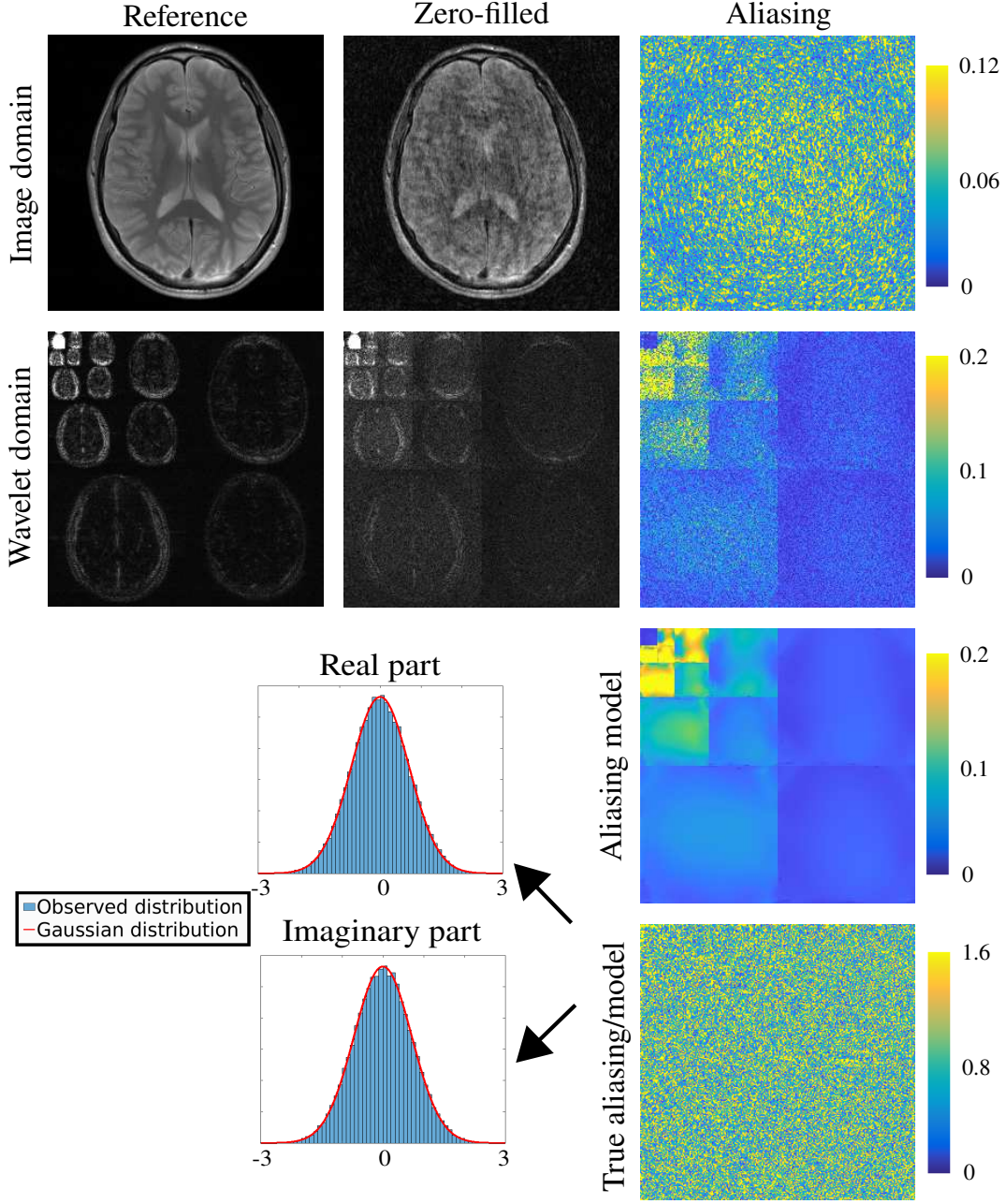


Figure 1: The density compensated, zero-filled estimate $\hat{\mathbf{x}}_0$ for a $R = 10$ Bernoulli undersampled 256×256 brain dataset. Here, $N_c = 16$ coils sensitivities were estimated with ESPIRiT⁴ via a 24×24 central autocalibration region and compressed to 8 virtual coils with Principle Component Analysis (PCA)⁴⁰, and an order 4 Daubechies wavelet Ψ at 4 decomposition scales was employed. The image labelled “Aliasing model” shows $\sqrt{\tau_0}$ computed via (3), and the image labelled “True aliasing/model” shows $\Psi(\mathbf{x}_0 - \hat{\mathbf{x}}_0) \oslash \sqrt{\tau_0}$, where \oslash is entry-wise division. The histograms show that the real and imaginary parts of the bottom-right image are distributed according to a white, zero-mean Gaussian: $\Psi(\mathbf{x}_0 - \hat{\mathbf{x}}_0) \oslash \sqrt{\tau_0} \sim \mathcal{CN}(\mathbf{0}, \mathbf{1}_N)$, which is equivalent to $\hat{\mathbf{x}}_0 \approx \mathbf{x}_0 + \mathcal{CN}(\mathbf{0}, \Psi \text{Diag}(\tau_0) \Psi^H)$. In other words, τ_0 accurately characterizes the aliasing of $\hat{\mathbf{x}}_0$.

where $\mathbb{E}\{\cdot\}$ is the expectation over the random Gaussian noise. Therefore cSURE can be minimised as a proxy for minimising the true squared error without requiring the ground truth \mathbf{w}_0 , so a near-optimal denoiser satisfying

$$\min_{\Theta} cSURE(\mathbf{f}(\mathbf{r}; \Theta); \tau) \approx \min_{\Theta} \|\mathbf{f}(\mathbf{r}; \Theta) - \mathbf{w}_0\|_2^2 \quad (8)$$

can be employed.

In this paper, as in single-coil VDAMP³⁵, we use the aliasing model (3) in conjunction with cSURE to employ soft thresholding with a per-subband threshold. To tune such a model by hand would be highly impractical; for instance, per-subband thresholding of a wavelet transform with 4 decomposition scales would require 13 parameters to be tuned by hand.

Statement of algorithm

The P-VDAMP algorithm is shown in Fig. 2. Lines 3-4, referred to as “density compensated gradient descent”, is gradient descent with a modified forward model that includes the sampling probability \mathbf{P} . Specifically, the modified forward model is comprised of (1) left-multiplied by $\mathbf{P}^{-1/2}$,

$$\mathbf{P}^{-1/2} \mathbf{y}_c = \mathbf{P}^{-1/2} \mathbf{M}_{\Omega} (\mathbf{F} \mathbf{S}_c \mathbf{x}_0 + \varepsilon_c), \quad (9)$$

for all coils. This weighting ensures that the columns of the multi-coil sensing matrix are normalized in expectation over the random mask, a necessary component of state evolution. At the first iteration $k = 0$, where $\tilde{\mathbf{r}}_0 = \mathbf{0}$, lines 3-4 correspond to the density-compensated zero-filled estimate stated in (2). Using density compensated gradient descent implies that the data consistency term in P-VDAMP’s cost function is a weighted ℓ_2 norm: $\sum_c \|\mathbf{P}^{-1/2}(\mathbf{y}_c - \mathbf{M}_{\Omega} \mathbf{F} \mathbf{S}_c \mathbf{x})\|_2^2$. The consequences of this are described in the Discussion section.

Lines 6-9 are identical to lines 6-9 of the single-coil VDAMP algorithm³⁵. In line 6, a function $\mathbf{g}(\mathbf{r}_k; \tau_k)$ is applied to the wavelet-domain estimate \mathbf{r}_k . Since, by state evolution, \mathbf{r}_k is the Gaussian corrupted ground truth, $\mathbf{g}(\mathbf{r}_k; \tau_k)$ is referred to as a *denoiser*. As described in the previous subsection, parameters of the denoiser can be tuned via cSURE using the aliasing model τ_k . Lines 7-9 correspond to a correction of the denoiser referred to in the AMP literature as “Onsager correction”, which removes the correlation that causes state evolution to fail for standard CS-MRI algorithms^{23,41}. In line 7, the notation $\langle \cdot \rangle_{\text{sband}}$ averages subbands, so that α_k has the structure

$$\alpha_k = \begin{bmatrix} \alpha_{k,1} \mathbf{1}_{N_1} \\ \alpha_{k,2} \mathbf{1}_{N_2} \\ \vdots \\ \alpha_{k,1+3s} \mathbf{1}_{N_{1+3s}} \end{bmatrix}, \quad (10)$$

with

$$\alpha_{k,b} = \frac{1}{N_b} \sum_{j \in J_b} \partial_j(\mathbf{g}(\mathbf{r}_k; \boldsymbol{\tau}_k)),$$

where J_b is the set of indices associated with subband b and $N_b = |J_b|$.

Line 11 of P-VDAMP gives two options for the algorithm output. The first uses gradient descent without density compensation. We also suggest $\boldsymbol{\Psi}^H \mathbf{r}_k$, which is unbiased when state evolution holds.

Algorithm P-VDAMP

Require: Sampling set Ω , coil sensitivities \mathbf{S}_c , wavelet transform $\boldsymbol{\Psi}$, probability matrix \mathbf{P} , measurements \mathbf{y}_c , measurement noise covariance $\boldsymbol{\Sigma}_\varepsilon^2$, denoiser $\mathbf{g}(\mathbf{r}; \boldsymbol{\tau})$, number of iterations K_{it} .

- 1: Compute $|\hat{\boldsymbol{\Psi}}|^2 = |\boldsymbol{\Psi} \mathbf{F}^H|^2$ and $\xi_{c,j} = \langle |\boldsymbol{\Psi}_j|^2, \text{Diag}(\mathbf{S}_c^H) \rangle$ and set $\tilde{\mathbf{r}}_0 = \mathbf{0}_N$
 - 2: **for** $k = 0, 1, \dots, K_{it} - 1$ **do**
 - 3: $\forall c, \mathbf{z}_{k,c} = \mathbf{y}_c - \mathbf{M}_\Omega \mathbf{F} \mathbf{S}_c \boldsymbol{\Psi}^H \tilde{\mathbf{r}}_k$
 - 4: $\mathbf{r}_k = \tilde{\mathbf{r}}_k + \boldsymbol{\Psi} \sum_c \mathbf{S}_c^H \mathbf{F}^H \mathbf{P}^{-1} \mathbf{z}_{k,c}$
 - 5: $\forall j, \tau_{k,j} = \boldsymbol{\xi}_j^H \left(\sum_i |\hat{\boldsymbol{\Psi}}_{ji}|^2 \left[\left(\frac{1-p_i}{p_i} \right) \mathbf{z}_{k,i} \mathbf{z}_{k,i}^H + \boldsymbol{\Sigma}_{\varepsilon,i}^2 \right] \frac{m_i}{p_i} \right) \boldsymbol{\xi}_j$
 - 6: $\hat{\mathbf{w}}_k = \mathbf{g}(\mathbf{r}_k; \boldsymbol{\tau}_k)$
 - 7: $\boldsymbol{\alpha}_k = \langle \partial(\mathbf{g}(\mathbf{r}_k; \boldsymbol{\tau}_k)) \rangle_{\text{sband}}$
 - 8: $\mathbf{c}_k = \mathbf{1}_N \oslash (\mathbf{1}_N - \boldsymbol{\alpha}_k)$
 - 9: $\tilde{\mathbf{r}}_{k+1} = \mathbf{c}_k \odot (\hat{\mathbf{w}}_k - \boldsymbol{\alpha}_k \odot \mathbf{r}_k)$
 - 10: **end for**
 - 11: **return** $\hat{\mathbf{x}} = \boldsymbol{\Psi}^H \hat{\mathbf{w}}_k + \sum_c \mathbf{S}_c^H \mathbf{F}^H (\mathbf{y}_c - \mathbf{M}_\Omega \mathbf{F} \mathbf{S}_c \boldsymbol{\Psi}^H \hat{\mathbf{w}}_k)$ or $\hat{\mathbf{x}} = \boldsymbol{\Psi}^H \mathbf{r}_k$
-

Figure 2: The P-VDAMP algorithm. Here, vectors with subscript c (\mathbf{y}_c and $\mathbf{z}_{k,c}$) refer to an N -dimensional vector on the c th coil, and vectors with subscript i or j ($\boldsymbol{\xi}_j$ and $\mathbf{z}_{k,i}$) refer to the N_c -dimensional vector at the i th or j th k-space coefficient. The function $\partial(\cdot)$ in line 7 is defined in (6). The notation \oslash in line 8 refers to entry-wise division and \odot in line 9 refers to entry-wise multiplication.

Methods

Description of data

P-VDAMP was evaluated on three types of MRI data:

- **Brain.** 256×256 acquisitions acquired on $N_c = 16$ coils, from an on-site Siemens 3T scanner.

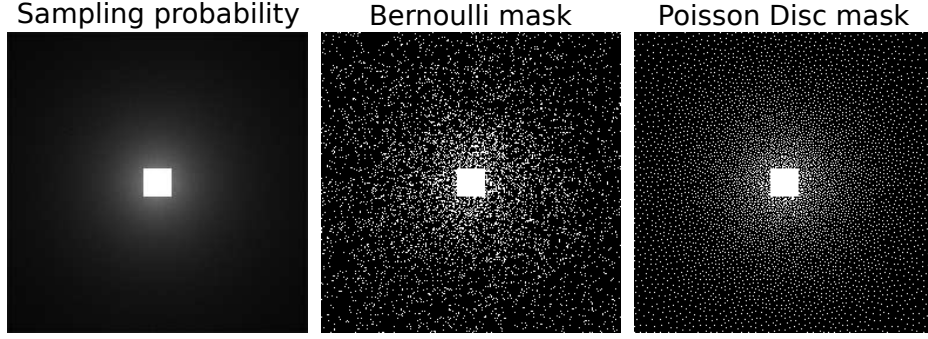


Figure 3: Sampling probability $\mathbf{P} = \mathbb{E}_{\Omega}\{\mathbf{M}_{\Omega}\}$ and associated Bernoulli and Poisson Disc masks \mathbf{M}_{Ω} for a 256×256 k-space at acceleration factor $R = 10$. To estimate the expectation \mathbf{P} , we computed the empirical mean of 10^4 instances of Poisson disc masks. The Bernoulli sampled masks were generated using the same \mathbf{P} .

- **Knee.** 368×640 acquisitions acquired on $N_c = 15$ coils, from the publicly available fastMRI dataset⁴², which includes a mixture of field strengths.
- **Time-of-flight Angiography.** $640 \times 506 \times 56$ acquisitions acquired on $N_c = 32$ coils, from an on-site Siemens 7T scanner, which we decomposed in to a series of 2D problems by taking an inverse Fourier transform along the first dimension.

For each of the three categories, we used two fully sampled datasets. The two knee datasets were randomly selected from the fastMRI dataset. All data were acquired in accordance with local ethics regulations.

Description of experimental method

All datasets were retrospectively undersampled at factors $R = 5, 10$ with both Bernoulli and Poisson disc masks. An example of the sampling probability and corresponding Bernoulli and Poisson Disc masks for a 256×256 k-space is shown in Fig. 3. The Poisson disc masks were generated using code from the ESPIRiT package (downloaded from <https://people.eecs.berkeley.edu/~mlustig/Software.html>) with a quadratically varying minimum distance between samples⁴³. All masks were fully sampled in a 24×24 central autocalibration region used to estimate the coil sensitivities \mathbf{S}_c with ESPIRiT⁴ via the BART toolbox³⁷.

To reduce the reconstruction time, the coils were compressed to 8 virtual coils with PCA⁴⁰: equation (3) is linear in N but quadratic in N_c , so P-VDAMP especially benefits from coil compression. For all algorithms we used the order 4 Daubechies mother wavelet at $s = 4$ decompositions scales for Ψ . Unless otherwise stated there was no additional measurement noise and the covariance Σ_{ϵ}^2 was set to a matrix of zeros.

Comments on P-VDAMP in practice

We have found that some damping aids P-VDAMP’s convergence, so that the denoiser is damped by a constant factor $0 < \rho \leq 1$. For $k > 0$, we suggest replacing lines 6 and 7 of P-VDAMP, Fig. 2 with

$$\begin{aligned}\hat{\mathbf{w}}_k &= \rho \mathbf{g}(\mathbf{r}_k; \boldsymbol{\tau}_k) + (1 - \rho) \hat{\mathbf{w}}_{k-1} \\ \boldsymbol{\alpha}_k &= \rho \langle \boldsymbol{\partial}(\mathbf{g}(\mathbf{r}_k; \boldsymbol{\tau}_k)) \rangle_{\text{sband}}.\end{aligned}$$

Note that $\rho = 1$ corresponds to zero damping. In all experiments in this paper, the damping factor was set to $\rho = 0.75$.

Rather than using a fixed number of iterations, we used a more practical stopping criterion based on the aliasing model $\boldsymbol{\tau}_k$.³⁹ In the experiments in this paper, P-VDAMP stops iterating when the mean-squared of the aliasing is predicted to have increased, $\langle \boldsymbol{\tau}_k \rangle > \langle \boldsymbol{\tau}_{k-1} \rangle$, or when $\langle \boldsymbol{\tau}_k \rangle$ changes by a small amount: $|\langle \boldsymbol{\tau}_k \rangle - \langle \boldsymbol{\tau}_{k-1} \rangle| / \langle \boldsymbol{\tau}_{k-1} \rangle < \epsilon$. We used $\epsilon = 10^{-3}$ throughout this paper.

Comparative algorithms

We evaluated the reconstruction quality of both output options in line 11 of P-VDAMP, Fig. 2, referring to the $\boldsymbol{\Psi}^H \mathbf{r}_k$ output as “Unbiased P-VDAMP”, and the alternative as simply “P-VDAMP”.

For comparative hand-tuned methods, we implemented the Fast Iterative Shrinkage-Thresholding algorithm (FISTA)⁴⁴ with a λ tuned using the reference to be approximately MSE optimal, referred to as “Optimal FISTA”. Secondly, to reflect the more realistic case where the sparse parameter is not optimally tuned, we also ran FISTA with a sparse weighting shared across all reconstructions, which we refer to as “Shared FISTA”. For the shared sparse weighting we used the mean of the optimally tuned sparse weightings.

For comparative tuning-free methods, we ran FISTA with a per-subband threshold tuned automatically with SURE using a white alising model, referred to as “SURE-IT”¹⁸. We also evaluated a recently proposed parameter-free variant of FISTA, which automatically selects a per-scale sparse weighting based on k-means clustering of the zero-filled estimate, referred to in this work as “Automatic-FISTA” (A-FISTA)¹⁹.

The stopping criteria employed for Optimal FISTA, Shared FISTA and SURE-IT was analogous to the P-VDAMP criteria described in the previous subsection. For A-FISTA, we found that such a stopping criterion typically stopped the algorithm prematurely, so to give A-FISTA the best chance of a high-quality reconstruction we used a fixed, large number of iterations. As in the original A-FISTA paper¹⁹, we chose 200 iterations.

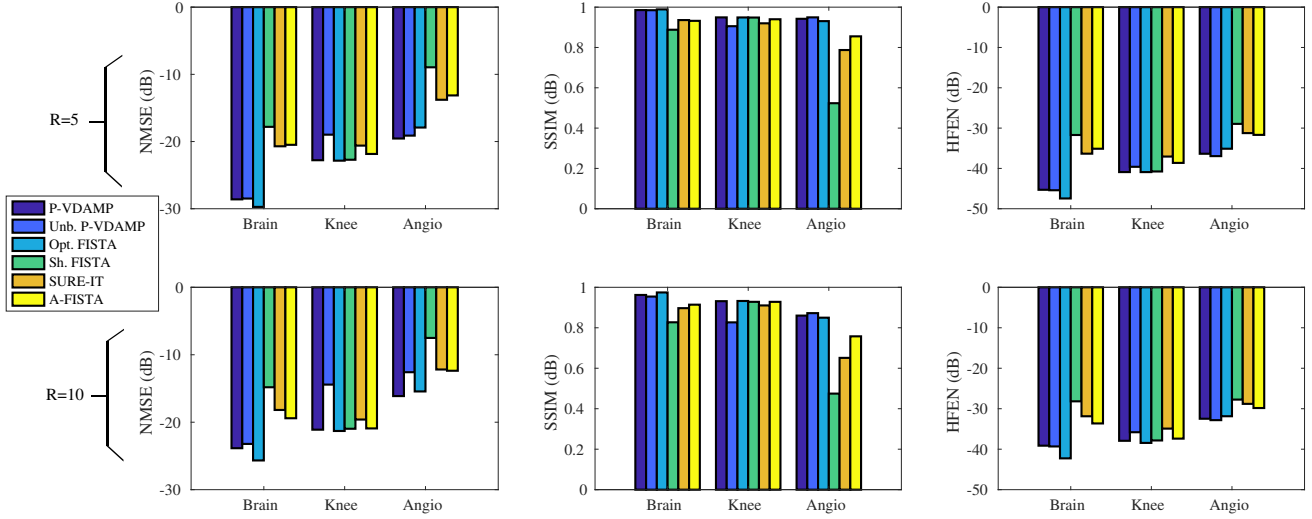


Figure 4: NMSE, SSIM and HFEN at $R = 5, 10$ for Bernoulli sampling, where the result for each datatype has been averaged over the two instances. Here, the HFEN has been normalised by dividing by the ℓ_2 norm of the reference image. P-VDAMP performs competitively with Optimal FISTA, and substantially outperforms the competing parameter-free methods SURE-IT and A-FISTA. P-VDAMP’s performance was similarly competitive for Poisson Disc sampling: see Supporting Information Fig. S1.

Performance metrics

Prior to computing performance metrics, we masked the images to mitigate background effects. For the brain and knee datasets, all pixels with absolute value less than 5% of the reference were masked. We also skull-stripped the angiograms with a hand-selected mask⁴⁵ and computed the maximum projection along the readout dimension.

To quantify reconstruction quality we used the Normalised Mean-Squared Error (NMSE), Structural Similarity Index Metric (SSIM)⁴⁶ and High-Frequency Error Norm (HFEN)⁴⁷, which quantifies the reconstruction quality of the image’s fine features. For the angiograms, we computed the SSIM after applying a vessel mask computed by thresholding with Otsu’s method^{48,49}.

Results

Reconstruction quality

The NMSE, HFEN and SSIM of each algorithm is shown in Fig. 4 for Bernoulli sampling and Supporting Information Fig. S1 for Poisson Disc sampling. P-VDAMP consistently outperformed the competing parameter-free methods, and was competitive with Optimal FISTA. Unbiased P-VDAMP’s NMSE and

SSIM was generally poorer than P-VDAMP, but had comparable HFEN.

Fig. 5 shows one of the Poisson Disc sampled brain datasets at $R = 5$. Optimal FISTA and both P-VDAMP estimates retain considerably more of the fine detail than competing methods. Shared FISTA’s λ is around 10 larger than Optimal FISTA in this case, and compression artifacts are clearly visible. The competing parameter-free methods SURE-IT and A-FISTA perform better than Shared FISTA in this case, but still have substantial reconstruction artifacts. The underlying anatomy is not clearly visible in Unbiased P-VDAMP’s error maps, with a similar contribution to the error at tissue boundaries and bulk tissue, which is a consequence of P-VDAMP’s state evolution.

One of the knee datasets Bernoulli undersampled at $R = 10$ is shown in Fig. 6. P-VDAMP outperforms both competing parameter-free methods, which smooth over details in the bone. Shared FISTA’s λ is 6 times smaller than Optimal FISTA here, and performs reasonably well, but still to a higher NMSE than P-VDAMP.

Fig. 7 shows the reconstructions of one of the Angiograms for $R = 5$ Poisson Disc sampled data, where P-VDAMP outperforms Optimal FISTA. The green arrow in the magnified region highlights a narrow region of a blood vessel, which is visible for Unbiased P-VDAMP and partially visible for P-VDAMP but mostly lost in the competing methods.

The τ_k update in line 5 of P-VDAMP, Fig. 2, is reasonably computationally expensive; P-VDAMP took around 4 times longer per iteration than FISTA in our MATLAB implementation. However, we found that P-VDAMP typically requires substantially fewer iterations, so required only a little longer than Optimal FISTA to reach convergence. This is illustrated in two NMSE vs time plots shown in Fig. 8.

P-VDAMP’s state evolution

Fig. 9 shows the wavelet-domain aliasing for one of the brain datasets Bernoulli sampled at $R = 10$ at iterations $k = 1, 2, 3$, which shows that state evolution approximately holds, $\hat{\mathbf{x}}_k \approx \mathbf{x}_0 + \mathcal{CN}(\mathbf{0}, \mathbf{\Psi} \text{Diag}(\boldsymbol{\tau}_k) \mathbf{\Psi}^H)$, beyond $k = 0$. There is a slight deviation from exactly unbiased aliasing apparent at $k = 2, 3$. This is due to P-VDAMP’s damping factor ρ , which causes P-VDAMP’s Onsager correction to be inexact. We found that using less damping caused state evolution to be more exact, but that the algorithm converged to a poorer reconstruction. We therefore recommend using damping at the cost of a slight breakdown in state evolution.

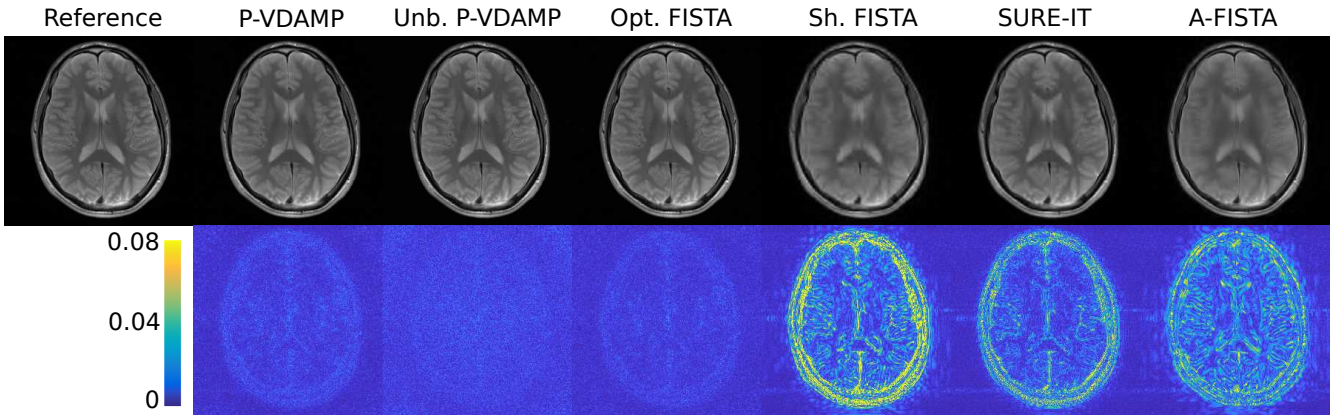


Figure 5: Reconstructions of a brain dataset Poisson Disc sampled with $R = 5$ with error maps. Shared FISTA’s sparse weighting is around a factor of 10 larger than for Optimal FISTA, which led to significant reconstruction artifacts. P-VDAMP performs competitively with Optimal FISTA and substantially better than the competing parameter-free methods SURE-IT and A-FISTA. The scale on the colorbar indicates that its maximum is 0.08 times the maximum of the reference image.

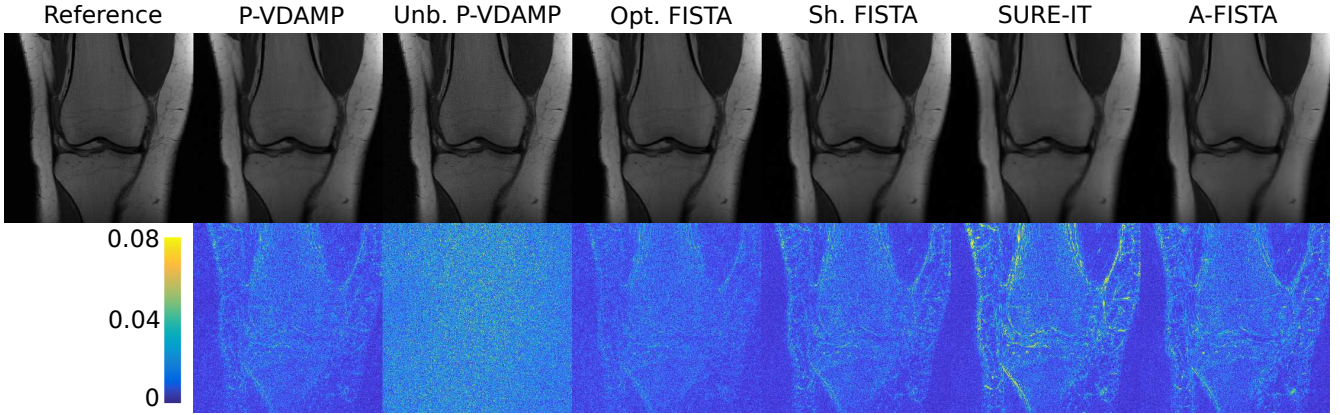


Figure 6: Reconstructions of a knee dataset Bernoulli sampled with $R = 10$, with error maps. Unbiased P-VDAMP’s NMSE is 2.5dB higher than the next worst, SURE-IT, but has competitive HFEN and performs well qualitatively

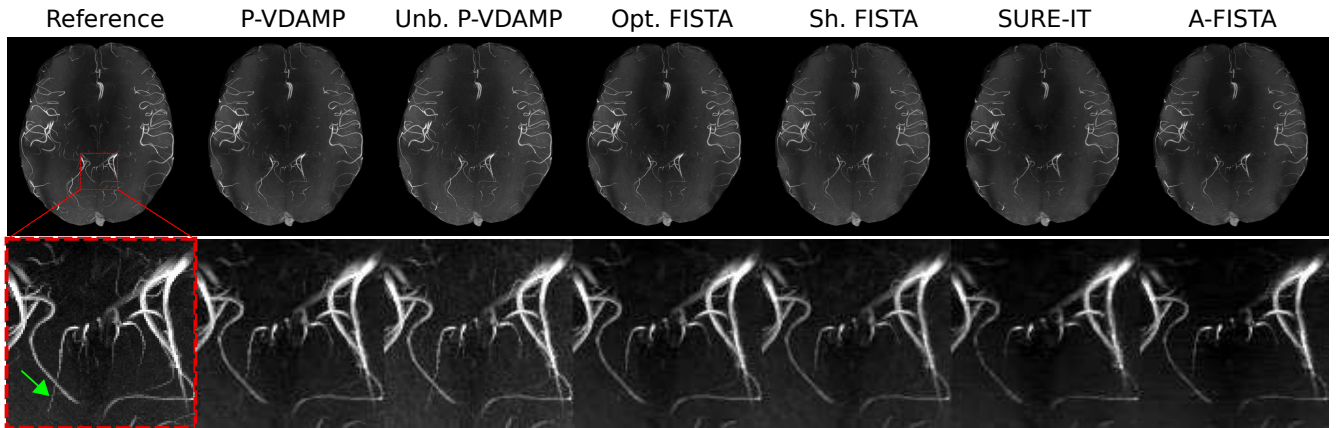


Figure 7: An angiogram Poisson Disc sampled with $R = 5$, with a magnified 100×100 region. The green arrow shows a challenging narrow blood vessel that is retained well for P-VDAMP and Unbiased P-VDAMP but mostly lost in competing methods.

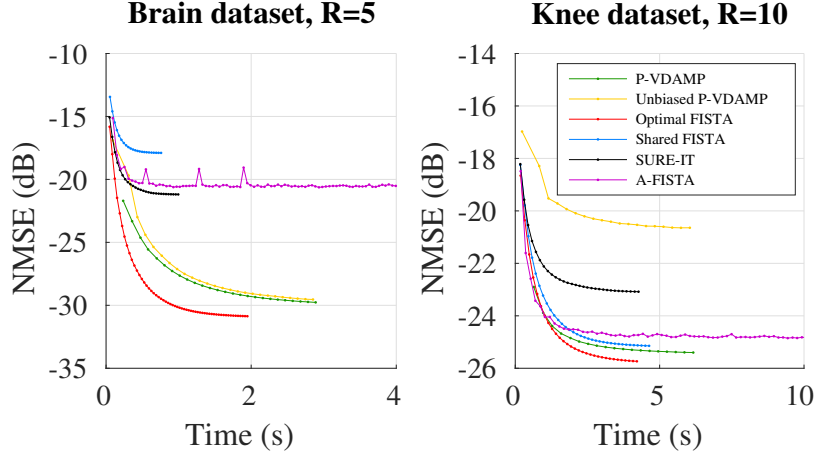


Figure 8: NMSE vs time for a Bernoulli sampled brain and knee dataset at $R = 5$ and $R = 10$ respectively. P-VDAMP is slightly outperformed by Optimal FISTA, but outperforms Shared FISTA, sometimes considerably, such as for the brain example shown in the left figure. P-VDAMP required substantially fewer iterations than FISTA, but usually required a little longer to converge due to its increased per-iteration computational cost. Optimal FISTA’s time to convergence here does not include the time to tune its sparse weighting, which was considerable.

Robustness to measurement noise

To evaluate the effect of measurement noise on P-VDAMP’s performance, we simulated Gaussian additive noise. We constructed an artificial measurement noise covariance matrix by generating a N_c -dimensional random vector \mathbf{v} with complex entries with real and imaginary parts drawn from a uniform distribution between -1 and 1 , and scaled the vector to $|\mathbf{v}| = c\mathbf{1}_{N_c}$, where c is a constant that determines the signal-to-noise ratio (SNR). For each measurement noise SNR we averaged over 10 random instances of \mathbf{v} . We compared P-VDAMP with FISTA with a fixed sparse weighting, tuned to be optimal in the absence of additional measurement noise.

Fig. 10 shows the dependence of the reconstruction NMSE on measurement noise SNR for each algorithm for one of the knee datasets Bernoulli sampled at $R = 10$. While FISTA’s sparse weighting is fixed, P-VDAMP’s sparse parameters adapt to the measurement noise on-the-fly and converges to a better solution for low SNR in this example. Unbiased P-VDAMP is more sensitive to measurement noise, and did not perform well for low SNR, indicating that it may not be appropriate for especially low SNR CS-MRI applications.

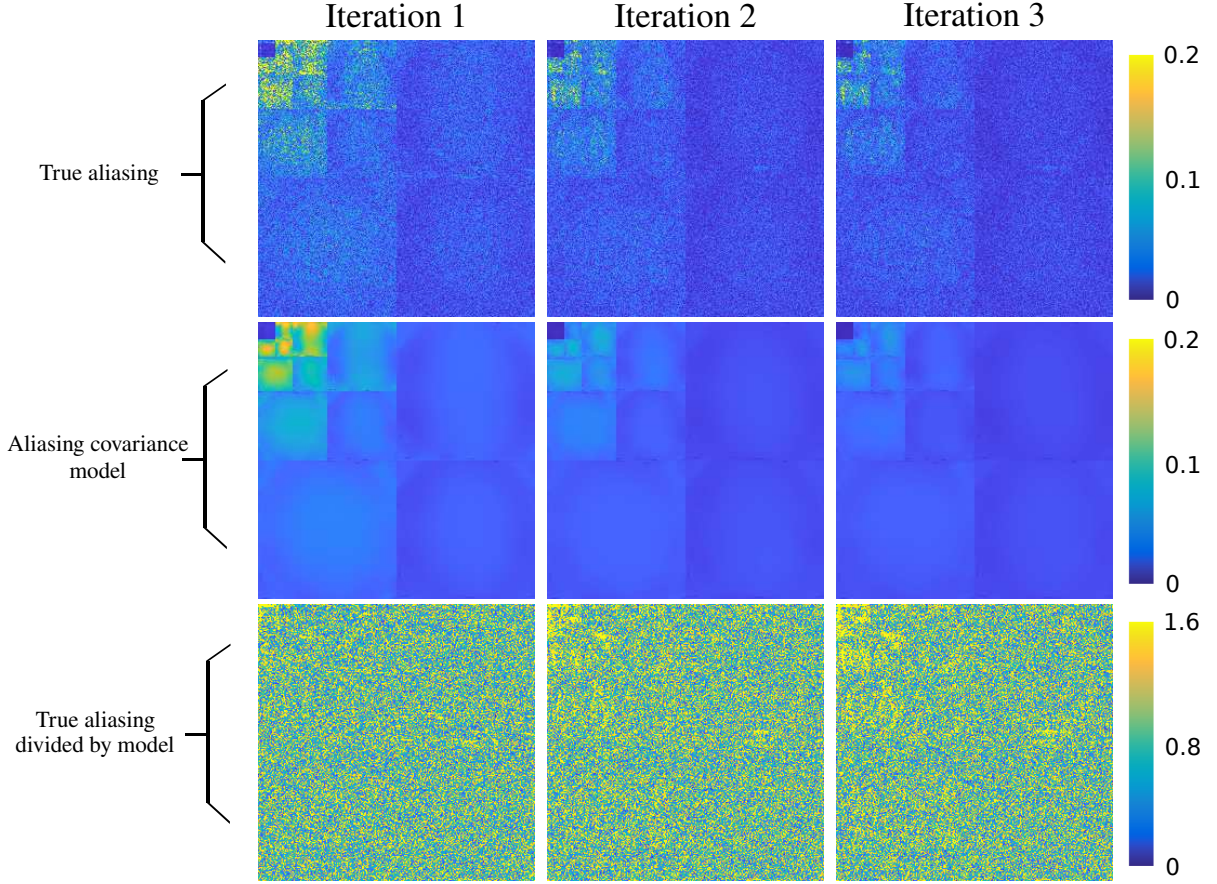


Figure 9: Demonstration of P-VDAMP’s state evolution for one of the brain datasets Bernoulli sampled at $R = 10$. The top row shows $|\mathbf{r}_k - \mathbf{w}_0|$, the middle row shows $\sqrt{\tau_k}$ and the bottom shows $|\mathbf{r}_k - \mathbf{w}_0| \oslash \sqrt{\tau_k}$ for iterations $k = 1, 2, 3$. The proximity of the bottom row to a white Gaussian indicates that $\hat{\mathbf{x}}_k \approx \mathbf{x}_0 + \mathcal{CN}(\mathbf{0}, \Psi \text{Diag}(\tau_k) \Psi^H)$ is an accurate model of the aliasing. In other words, the behaviour shown at $k = 0$ in Fig. 1 holds for subsequent iterations. A similar figure for Poisson Disc sampling is shown in the Supporting Information Fig. S.2.

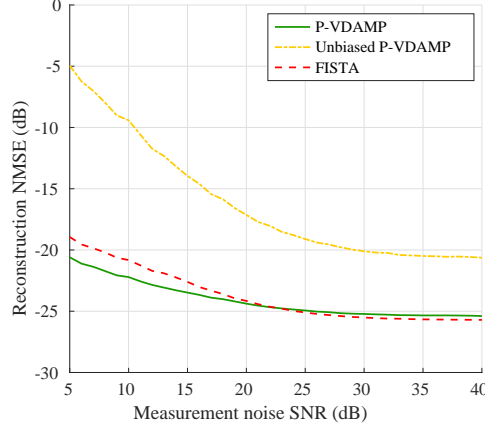


Figure 10: The reconstruction NMSE of P-VDAMP, Unbiased P-VDAMP and FISTA with a fixed sparse weighting as a function of simulated measurement noise SNR for one of the knee datasets Bernoulli sampled at $R = 10$. P-VDAMP’s sparse parameters automatically adapt to measurement noise, so outperforms FISTA for low SNR, where FISTA’s weighting is poorly tuned. Unbiased P-VDAMP is more sensitive to measurement noise, and does not perform well in the low SNR regime.

Discussion

The highly mixed performance of Shared FISTA emphasizes that the choice of sparse weighting is key, and that sharing its value for different types of data cannot be expected to yield a consistently high quality reconstruction. We found that P-VDAMP performed competitively with Optimal FISTA for all reconstructions, indicating that it is robust to the forward model and anatomy. Since the fully sampled reference is not available for parameter tuning in prospectively undersampled scans, FISTA’s parameter tuning cannot be expected to be near-optimal, so P-VDAMP is likely to outperform FISTA in practice.

P-VDAMP consistently outperformed the competing parameter-free methods SURE-IT and A-FISTA. The improvement over SURE-IT emphasises that P-VDAMP’s state evolution is key for high-quality threshold selection with SURE. A-FISTA’s performance is quite mixed, which indicates that the quality of its parameter tuning is not as robust as P-VDAMP.

Since P-VDAMP’s sparse model has one parameter per subband while Optimal FISTA has a single, global parameter, one might expect that P-VDAMP would consistently outperform Optimal FISTA. There are two reasons why P-VDAMP does not always outperform Optimal FISTA. Firstly, P-VDAMP’s \mathbf{P}^{-1} in lines 3-4 of Fig. 2, which is essential for state evolution, is not advantageous from a reconstruction error perspective as it boosts errors at high frequencies, where the sampling probability is low. P-VDAMP outperforms Optimal FISTA when the benefits of its richer sparse model “wins” over the disadvantage of needing to include \mathbf{P}^{-1} . The second reason is that damping causes P-VDAMP’s aliasing model τ_k to be

imperfect, especially for high k , as illustrated in Fig. 9, so parameter selection with SURE is not always near-optimal in practice.

Although P-VDAMP performed well for Bernoulli and Poisson Disc sampling, we have found that it typically diverges when naively applied to problems that contain smooth sampling trajectories, so cannot yet be applied to sampling schemes such as 3D radial⁵⁶ or 3D cones⁵⁷, nor to purely 2D acquisitions. The proposals in this paper could be extended to such sampling schemes by an appropriate modification of the aliasing model in line 5 of P-VDAMP, Fig. 2.

Very recently an AMP-based algorithm was proposed⁵⁸ for single and multi-coil MRI acquisitions that uses similar principles to single-coil VDAMP but with an alternative procedure for data consistency at each iteration, which may have better fixed points. Extending the richer aliasing model presented in this paper to the multi-coil version of this alternative algorithm is a desirable avenue for future work.

Conclusions

State evolution essentially recasts multi-coil CS-MRI reconstruction as a sequence of Gaussian denoising tasks, where the Gaussian “effective noise” has known distribution parameters. In other words, roughly speaking, how well one can reconstruct an image depends on how well one can denoise a Gaussian-corrupted version of it³⁰. This suggests a number of potential advantages of P-VDAMP’s state evolution beyond parameter tuning that could be explored in future work. For instance, benefits for deep-learning based reconstruction^{39,50,51} and uncertainty quantification⁵² have already been explored in the context of single-coil VDAMP³⁹. Initial work by the authors on Denoising-P-VDAMP (D-P-VDAMP)⁵³ has shown that the deep Plug-and-Play framework^{54,55} can improve P-VDAMP’s performance on the fastMRI dataset⁴².

P-VDAMP is an efficient, robust and principled tuning-free algorithm for CS-MRI that is competitive with Optimal FISTA and offers substantial robustness and reconstruction quality improvements over competing parameter-free methods.

Acknowledgements

We are grateful to Thijs de Buck for sharing his angiography data. This work was supported in part by an EPSRC Industrial CASE studentship with Siemens Healthineers under voucher 17000051, in part by The Alan Turing Institute under EPSRC grant EP/N510129/1, in part by EPSRC under grant EP/T013133/1, in part by the Royal Academy of Engineering under grant RF201617/16/23, and in part by the Wellcome Trust under grant 203139/Z/16/Z. The concepts and information presented in this paper are based on

research results that are not commercially available.

Appendix: error propagation formula

This appendix derives an approximate expression for the diagonal of the covariance of the aliasing of $\mathbf{r}_0 = \Psi \hat{\mathbf{x}}_0$, where $\hat{\mathbf{x}}_0 = \sum_c \mathbf{S}_c^H \mathbf{F}^H \mathbf{P}^{-1} \mathbf{y}_c$. Let $\mathbf{y}_{0,c} = \mathbf{F} \mathbf{S}_c \mathbf{x}_0$ be the signal of interest's coil-weighted Fourier coefficients. Using $\mathbf{x}_0 = \sum_c \mathbf{S}_c^H \mathbf{F}^H \mathbf{y}_{0,c}$, the aliasing of \mathbf{r}_0 is

$$\begin{aligned} |\mathbf{r}_0 - \mathbf{w}_0|^2 &= |\Psi(\hat{\mathbf{x}}_0 - \mathbf{x}_0)|^2 \\ &= |\Psi \sum_c \mathbf{S}_c^H \mathbf{F}^H [\mathbf{P}^{-1} \mathbf{y}_c - \mathbf{y}_{0,c}]|^2 \\ &= |\sum_c \hat{\Psi}^c [\mathbf{P}^{-1} \mathbf{y}_c - \mathbf{y}_{0,c}]|^2, \end{aligned}$$

where $\hat{\Psi}^c = \Psi \mathbf{S}_c^H \mathbf{F}^H$. Since $\mathbf{y}_c = \mathbf{M}_\Omega(\mathbf{y}_{0,c} + \boldsymbol{\varepsilon}_c)$,

$$\begin{aligned} |\sum_c \hat{\Psi}^c [\mathbf{P}^{-1} \mathbf{y}_c - \mathbf{y}_{0,c}]|^2 &= |\sum_c \hat{\Psi}^c [(\mathbf{P}^{-1} \mathbf{M}_\Omega - \mathbb{1}) \mathbf{y}_{0,c} - \mathbf{P}^{-1} \mathbf{M}_\Omega \boldsymbol{\varepsilon}_c]|^2 \\ &= |\sum_c \hat{\Psi}^c \mathbf{q}_c|^2 \end{aligned} \quad (11)$$

where we define $\mathbf{q}_c = (\mathbf{P}^{-1} \mathbf{M}_\Omega - \mathbb{1}) \mathbf{y}_{0,c} - \mathbf{P}^{-1} \mathbf{M}_\Omega \boldsymbol{\varepsilon}_c$.

Computing the expectation of (11) with a method analogous to the single-coil approach³⁵ would involve computing and storing in memory the $N \times N$ matrices $|\Psi^c|^2$ for all N_c coils, which is not practical for large N . We suggest approximating the $\hat{\Psi}^c$ in terms of the unweighted spectra $\hat{\Psi} = \Psi \mathbf{F}^H$, so that the spectral density of the j th row of $\hat{\Psi}^c$ is expressed as

$$\hat{\Psi}_j^c \approx \xi_{c,j} \hat{\Psi}_j, \quad (12)$$

where $\xi_{c,j} \in \mathbb{C}$ is a constant. Since $\hat{\Psi}_j^c$ is the j th coil-weighted wavelet spectrum, (12) is interpretable as approximating the coil sensitivity as flat over the support of the j th wavelet filter, so that its spectrum is the unweighted spectrum multiplied by a filter- and coil-dependent scalar. We suggest using the $\xi_{c,j}$ that minimises $\|\hat{\Psi}_j^c - \xi_{c,j} \hat{\Psi}_j\|_2^2$:

$$\begin{aligned} \xi_{c,j} &= \arg \min_{\xi} \|\hat{\Psi}_j^c - \xi \hat{\Psi}_j\|_2^2 \\ &= \arg \min_{\xi} \|\Psi_j \mathbf{S}_c^H \mathbf{F}^H - \xi \Psi_j \mathbf{F}^H\|_2^2 \\ &= \frac{\Psi_j \mathbf{S}_c^H \Psi_j^H}{\Psi_j \Psi_j^H} \\ &= \langle |\Psi_j|^2, \text{Diag}(\mathbf{S}_c^H) \rangle, \end{aligned}$$

where Ψ_j is the j th row of Ψ , and we have used the orthonormality of the rows of Ψ_j to set $\Psi_j \Psi_j^H = 1$.

Claim 1. Let $\xi_{c,j} \in \mathbb{C}$ be a constant that approximates $\hat{\Psi}_j^c \approx \xi_{c,j} \hat{\Psi}_j$, for all j rows of $\hat{\Psi}^c$. Then the expectation of (11) is

$$\mathbb{E}\{|r_{0,j} - w_{0,j}|^2\} \approx \xi_j^H \left(\sum_i |\hat{\Psi}_{ji}|^2 \left[\left(\frac{1-p_i}{p_i} \right) \mathbf{y}_{0,i} \mathbf{y}_{0,i}^H + \frac{1}{p_i} \Sigma_{\varepsilon,i}^2 \right] \right) \xi_j, \quad (13)$$

where the $\mathbf{y}_{0,i} \in \mathbb{C}^{N_c}$ and $\xi_{0,j} \in \mathbb{C}^{N_c}$ are comprised of the i th k-space location over all coils, having c th entry $[y_{0,i}]_c = [\mathbf{F} \mathbf{S}_c \mathbf{x}_0]_i$ and $[\xi_{0,j}]_c = \xi_{c,j}$, and $\Sigma_{\varepsilon,i}^2 = \mathbb{E}\{\varepsilon_i \varepsilon_i^H\}$ where $\varepsilon_i \in \mathbb{C}^{N_c}$ similarly has c th entry $\varepsilon_{i,c} = [\varepsilon_c]_i$.

Proof. Using (12), the j th entry of (11) is approximately

$$|r_{0,j} - w_{0,j}|^2 \approx \left| \sum_c \hat{\Psi}_j \mathbf{q}_c \xi_{c,j} \right|^2 \quad (14a)$$

$$= \left| \sum_{c,i} \hat{\Psi}_{ji} q_{c,i} \xi_{c,j} \right|^2. \quad (14b)$$

Using the result from Appendix C of the single-coil VDAMP paper³⁵, the expectation of (14b) over the sampling mask and measurement noise is

$$\mathbb{E}\left\{ \left| \sum_{c,i} \hat{\Psi}_{ji} q_{c,i} \xi_{c,j} \right|^2 \right\} = \sum_i |\hat{\Psi}_{ji}|^2 \mathbb{E}\left\{ \left| \sum_c \xi_{c,j} q_{c,i} \right|^2 \right\} \quad (15a)$$

$$= \sum_i |\hat{\Psi}_{ji}|^2 \mathbb{E}\{ |\xi_j^H \mathbf{q}_i|^2 \}, \quad (15b)$$

where $\xi_j \in \mathbb{C}^{N_c}$ and $\mathbf{q}_i \in \mathbb{C}^{N_c}$. Resolving the expectation,

$$\mathbb{E}\{ |\xi_j^H \mathbf{q}_i|^2 \} = \mathbb{E}\{ \xi_j^H \mathbf{q}_i \mathbf{q}_i^H \xi_j \} \quad (16a)$$

$$= \mathbb{E} \left\{ \xi_j^H \left[\left(\frac{m_i}{p_i} - 1 \right)^2 \mathbf{y}_{0,i} \mathbf{y}_{0,i}^H + \left(\frac{m_i}{p_i} \right)^2 \varepsilon_i \varepsilon_i^H \right] \xi_j \right\}, \quad (16b)$$

where $\mathbb{E}\{\varepsilon_i\} = \mathbf{0}_{N_c}$ has been applied to evaluate the cross-terms to zero. For Bernoulli sampling,

$$\mathbb{E} \left\{ \left(\frac{m_i}{p_i} - 1 \right)^2 \right\} = \frac{1-p_i}{p_i}, \quad \mathbb{E}\{\varepsilon_i \varepsilon_i^H\} = \Sigma_{\varepsilon,i}^2,$$

so (16b) is

$$\mathbb{E}\{ |\xi_j^H \mathbf{q}_i|^2 \} = \xi_j^H \left[\left(\frac{1-p_i}{p_i} \right) \mathbf{y}_{0,i} \mathbf{y}_{0,i}^H + \frac{1}{p_i} \Sigma_{\varepsilon,i}^2 \right] \xi_j. \quad (17)$$

Substituting (17) in to (15b) gives

$$\mathbb{E}\{|r_{0,j} - w_{0,j}|^2\} \approx \sum_i |\hat{\Psi}_{ji}|^2 \xi_j^H \left[\left(\frac{1-p_i}{p_i} \right) \mathbf{y}_{0,i} \mathbf{y}_{0,i}^H + \frac{1}{p_i} \Sigma_{\varepsilon,i}^2 \right] \xi_j,$$

which is equal to (13). \square

Eqn. (13) requires knowledge of \mathbf{y}_0 so is of limited practical use. However, we can approximate $\mathbb{E}_{\Omega, \varepsilon}\{|r_{0,j} - w_{0,j}|^2\}$ without the ground truth with

$$\tau_j = \boldsymbol{\xi}_j^H \left(\sum_i |\hat{\Psi}_{ji}|^2 \left[\left(\frac{1-p_i}{p_i} \right) \mathbf{y}_i \mathbf{y}_i^H + \boldsymbol{\Sigma}_{\varepsilon,i}^2 \right] \frac{m_i}{p_i} \right) \boldsymbol{\xi}_j. \quad (18)$$

Claim 2. The estimate of the multi-coil wavelet-domain error stated in (18) is unbiased:

$$\mathbb{E}\{\tau_j\} = \boldsymbol{\xi}_j^H \left(\sum_i |\hat{\Psi}_{ji}|^2 \left[\left(\frac{1-p_i}{p_i} \right) \mathbf{y}_{0,i} \mathbf{y}_{0,i}^H + \frac{1}{p_i} \boldsymbol{\Sigma}_{\varepsilon,i}^2 \right] \right) \boldsymbol{\xi}_j. \quad (19)$$

Proof. Since $\mathbf{y}_i = m_i(\mathbf{y}_{0,i} + \boldsymbol{\varepsilon}_i)$, and using $\mathbb{E}\{\boldsymbol{\varepsilon}_i\} = \mathbf{0}_{N_c}$,

$$\begin{aligned} & \mathbb{E} \left\{ \left[\left(\frac{1-p_i}{p_i} \right) \mathbf{y}_i \mathbf{y}_i^H + \boldsymbol{\Sigma}_{\varepsilon,i}^2 \right] \frac{m_i}{p_i} \right\} \\ &= \mathbb{E} \left\{ \left[m_i \left(\frac{1-p_i}{p_i} \right) (\mathbf{y}_{0,i} \mathbf{y}_{0,i}^H + \boldsymbol{\varepsilon}_i \mathbf{y}_{0,i}^H + \mathbf{y}_{0,i} \boldsymbol{\varepsilon}_i^H + \boldsymbol{\varepsilon}_i \boldsymbol{\varepsilon}_i^H) + \boldsymbol{\Sigma}_{\varepsilon,i}^2 \right] \frac{m_i}{p_i} \right\} \\ &= \left(\frac{1-p_i}{p_i} \right) \mathbf{y}_{0,i} \mathbf{y}_{0,i}^H + \frac{1}{p_i} \boldsymbol{\Sigma}_{\varepsilon,i}^2 \end{aligned} \quad (20)$$

Substituting (20) in (18) gives the right-hand-side of (19). \square

References

- [1] Jong Beom Ra and C Y Rim. Fast imaging using subencoding data sets from multiple detectors. *Magnetic resonance in medicine*, 30(1):142–145, 1993.
- [2] K P Pruessmann, M Weiger, M B Scheidegger, and P Boesiger. SENSE: sensitivity encoding for fast MRI. *Magnetic resonance in medicine*, 42(5):952–62, nov 1999.
- [3] Mark A. Griswold, Peter M. Jakob, Robin M. Heidemann, Mathias Nittka, Vladimir Jellus, Jianmin Wang, Berthold Kiefer, and Axel Haase. Generalized autocalibrating partially parallel acquisitions (GRAPPA). *Magnetic Resonance in Medicine*, 47(6):1202–1210, jun 2002.
- [4] Martin Uecker, Peng Lai, Mark J. Murphy, Patrick Virtue, Michael Elad, John M. Pauly, Shreyas S. Vasanawala, and Michael Lustig. ESPIRiT—an eigenvalue approach to autocalibrating parallel MRI: Where SENSE meets GRAPPA. *Magnetic Resonance in Medicine*, 71(3):990–1001, mar 2014.
- [5] Emmanuel Candes, Justin Romberg, and Terence Tao. Robust uncertainty principles: exact signal reconstruction from highly incomplete frequency information. *IEEE Transactions on Information Theory*, 52(2):489–509, feb 2006.
- [6] David L Donoho. Compressed sensing. *IEEE Transactions on Information Theory*, 52(4):1289–1306, apr 2006.

- [7] Michael Lustig, David Donoho, and John M. Pauly. Sparse MRI: The application of compressed sensing for rapid MR imaging. *Magnetic Resonance in Medicine*, 58(6):1182–1195, dec 2007.
- [8] Dong Liang, Bo Liu, JiunJie Wang, and Leslie Ying. Accelerating SENSE using compressed sensing. *Magnetic Resonance in Medicine*, 62(6):1574–1584, dec 2009.
- [9] Mark Murphy, Marcus Alley, James Demmel, Kurt Keutzer, Shreyas Vasanaawala, and Michael Lustig. Fast l1-SPIRiT compressed sensing parallel imaging MRI: scalable parallel implementation and clinically feasible runtime. *IEEE transactions on medical imaging*, 31(6):1250–62, jun 2012.
- [10] Albert Hsiao, Michael Lustig, Marcus T. Alley, Mark Murphy, Frandics P. Chan, Robert J. Herfkens, and Shreyas S. Vasanaawala. Rapid pediatric cardiac assessment of flow and ventricular volume with compressed sensing parallel imaging volumetric cine phase-contrast MRI. *American Journal of Roentgenology*, 198(3):W250–W259, mar 2012.
- [11] Kieren G. Hollingsworth, David M. Higgins, Michelle McCallum, Louise Ward, Anna Coombs, and Volker Straub. Investigating the quantitative fidelity of prospectively undersampled chemical shift imaging in muscular dystrophy with compressed sensing and parallel imaging reconstruction. *Magnetic Resonance in Medicine*, 72(6):1610–1619, dec 2014.
- [12] Thai Akasaka, Koji Fujimoto, Takayuki Yamamoto, Tomohisa Okada, Yasutaka Fushumi, Akira Yamamoto, Toshiyuki Tanaka, and Kaori Togashi. Optimization of regularization parameters in compressed sensing of magnetic resonance angiography: Can statistical image metrics mimic radiologists’ perception? *PLOS ONE*, 11(1):1–14, 01 2016.
- [13] Oren N Jaspan, Roman Fleysheer, and Michael L Lipton. Compressed sensing MRI: a review of the clinical literature. *The British Journal of Radiology*, 88(1056):20150487, dec 2015.
- [14] Per Christian Hansen. The L-curve and its use in the numerical treatment of inverse problems. 1999.
- [15] Sathish Ramani, Zhihao Liu, Jeffrey Rosen, Jon-Fredrik Nielsen, and Jeffrey A Fessler. Regularization parameter selection for nonlinear iterative image restoration and MRI reconstruction using GCV and SURE-based methods. *IEEE Transactions on Image Processing*, 21(8):3659–3672, 2012.
- [16] Raja Giryes, Michael Elad, and Yonina C Eldar. The projected GSURE for automatic parameter tuning in iterative shrinkage methods. *Applied and Computational Harmonic Analysis*, 30(3):407–422, 2011.

- [17] Daniel S Weller, Sathish Ramani, Jon-Fredrik Nielsen, and Jeffrey A Fessler. Monte Carlo SURE-based parameter selection for parallel magnetic resonance imaging reconstruction. *Magnetic Resonance in Medicine*, 71(5):1760–1770, 2014.
- [18] Kedar Khare, Christopher J. Hardy, Kevin F. King, Patrick A. Turski, and Luca Marinelli. Accelerated MR imaging using compressive sensing with no free parameters. *Magnetic Resonance in Medicine*, 68(5):1450–1457, nov 2012.
- [19] Gabriel Varela-Mattatall, Corey A Baron, and Ravi S Menon. Automatic determination of the regularization weighting for wavelet-based compressed sensing MRI reconstructions. *Magnetic Resonance in Medicine*, 2021.
- [20] Charles M. Stein. Estimation of the Mean of a Multivariate Normal Distribution. *The Annals of Statistics*, 9(6):1135–1151, nov 1981.
- [21] David L. Donoho and Iain M. Johnstone. Adapting to Unknown Smoothness via Wavelet Shrinkage. *Journal of the American Statistical Association*, 90(432):1200, dec 1995.
- [22] Frank Ong, Martin Uecker, Umar Tariq, Albert Hsiao, Marcus T Alley, Shreyas S. Vasanawala, and Michael Lustig. Robust 4D Flow Denoising Using Divergence-Free Wavelet Transform. *Magnetic Resonance in Medicine*, 73(2):828, feb 2015.
- [23] David L Donoho, Arian Maleki, and Andrea Montanari. Message-passing algorithms for compressed sensing. *Proceedings of the National Academy of Sciences*, 106(45):18914–18919, 2009.
- [24] Ali Mousavi, Arian Maleki, and Richard G. Baraniuk. Parameterless Optimal Approximate Message Passing. *arXiv preprint arXiv:1311.0035*, oct 2013.
- [25] Chunli Guo and Mike E. Davies. Near Optimal Compressed Sensing Without Priors: Parametric SURE Approximate Message Passing. *IEEE Transactions on Signal Processing*, 63(8):2130–2141, apr 2015.
- [26] Mohsen Bayati, Murat A. Erdogdu, and Andrea Montanari. Estimating LASSO risk and noise level. *Advances in Neural Information Processing Systems*, pages 1–9, 2013.
- [27] Mohsen Bayati and Andrea Montanari. The Dynamics of Message Passing on Dense Graphs, with Applications to Compressed Sensing. *IEEE Transactions on Information Theory*, 57(2):764–785, feb 2011.

- [28] Kyunghyun Sung, Bruce L Daniel, and Brian A Hargreaves. Location Constrained Approximate Message Passing for Compressed Sensing MRI. *Magnetic Resonance in Medicine*, 70:370–381, 2013.
- [29] Ender M. Eksioğlu and A. Korhan Tanc. Denoising AMP for MRI Reconstruction: BM3D-AMP-MRI. *SIAM Journal on Imaging Sciences*, 11(3):2090–2109, jan 2018.
- [30] Christopher A. Metzler, Arian Maleki, and Richard G. Baraniuk. From Denoising to Compressed Sensing. *IEEE Transactions on Information Theory*, 62(9):5117–5144, 2016.
- [31] Hanvit Kim, Dong Un Kang, and Se Young Chun. Preliminary Studies On Training And Fine-Tuning Deep Denoiser Neural Networks In Learned D-Amp For Undersampled Real Mr Measurements. In *2020 IEEE 17th International Symposium on Biomedical Imaging Workshops (ISBI Workshops)*, pages 1–4, 2020.
- [32] Sundeep Rangan, Philip Schniter, and Alyson K. Fletcher. Vector Approximate Message Passing. *IEEE Transactions on Information Theory*, pages 1–1, 2019.
- [33] Philip Schniter, Sundeep Rangan, and Alyson Fletcher. Plug-and-play Image Recovery using Vector AMP. *BASP Frontiers Workshop 2017*, 2017.
- [34] Subrata Sarkar, Rizwan Ahmad, and Philip Schniter. MRI Image Recovery using Damped Denoising Vector AMP. (2):1–5, 2020.
- [35] C Millard, A T Hess, B Mailhe, and J Tanner. Approximate Message Passing with a Colored Aliasing Model for Variable Density Fourier Sampled Images. *IEEE Open Journal of Signal Processing*, page 1, 2020.
- [36] C Millard, A T Hess, B Mailhe, and J Tanner. An Approximate Message Passing Algorithm For Rapid Parameter-Free Compressed Sensing MRI. In *2020 IEEE International Conference on Image Processing (ICIP)*, pages 91–95, 2020.
- [37] Martin Uecker, Jonathan I Tamir, Frank Ong, and Michael Lustig. The BART Toolbox for Computational Magnetic Resonance Imaging. In *ISMRM*, 2016.
- [38] Patrick Virtue and Michael Lustig. The Empirical Effect of Gaussian Noise in Undersampled MRI Reconstruction. *Tomography*, 3(4):211–221, dec 2017.
- [39] Christopher A. Metzler and Gordon Wetzstein. D-VDAMP: Denoising-based Approximate Message Passing for Compressive MRI. *arXiv:2010.13211*, 2020.

- [40] Feng Huang, Sathya Vijayakumar, Yu Li, Sarah Hertel, and George R. Duensing. A software channel compression technique for faster reconstruction with many channels. *Magnetic Resonance Imaging*, 26(1):133–141, 2008.
- [41] Junjie Ma and Li Ping. Orthogonal AMP. *IEEE Access*, 5:2020–2033, 2017.
- [42] Jure Zbontar, Florian Knoll, Anuroop Sriram, Tullie Murrell, Zhengnan Huang, Matthew J Muckley, Aaron Defazio, Ruben Stern, Patricia Johnson, Mary Bruno, et al. fastMRI: An open dataset and benchmarks for accelerated MRI. *arXiv preprint arXiv:1811.08839*, 2018.
- [43] Robert Bridson. Fast Poisson disk sampling in arbitrary dimensions. *SIGGRAPH sketches*, 10:1, 2007.
- [44] Amir Beck and Marc Teboulle. A Fast Iterative Shrinkage-Thresholding Algorithm for Linear Inverse Problems. *SIAM Journal on Imaging Sciences*, 2(1):183–202, jan 2009.
- [45] P Kalavathi and VB Surya Prasath. Methods on skull stripping of MRI head scan images—a review. *Journal of digital imaging*, 29(3):365–379, 2016.
- [46] Zhou Wang, Alan Conrad Bovik, Hamid Rahim Sheikh, and Eero P. Simoncelli. Image quality assessment: From error visibility to structural similarity. *IEEE Transactions on Image Processing*, 13(4):600–612, 2004.
- [47] Saiprasad Ravishankar and Yoram Bresler. MR image reconstruction from highly undersampled k-space data by dictionary learning. *IEEE transactions on medical imaging*, 30(5):1028–1041, 2010.
- [48] Nobuyuki Otsu. A threshold selection method from gray-level histograms. *IEEE transactions on systems, man, and cybernetics*, 9(1):62–66, 1979.
- [49] Thai Akasaka, Koji Fujimoto, Takayuki Yamamoto, Tomohisa Okada, Yasutaka Fushumi, Akira Yamamoto, Toshiyuki Tanaka, and Kaori Togashi. Optimization of regularization parameters in compressed sensing of magnetic resonance angiography: can statistical image metrics mimic radiologists’ perception? *PloS one*, 11(1):146548, 2016.
- [50] Chris Metzler, Ali Mousavi, and Richard Baraniuk. Learned D-AMP: Principled Neural Network based Compressive Image Recovery. In I Guyon, U V Luxburg, S Bengio, H Wallach, R Fergus, S Vishwanathan, and R Garnett, editors, *Advances in Neural Information Processing Systems 30*, pages 1772–1783. Curran Associates, Inc., 2017.

- [51] Mark Borgerding, Philip Schniter, and Sundeep Rangan. AMP-inspired deep networks for sparse linear inverse problems. *IEEE Transactions on Signal Processing*, 65(16):4293–4308, 2017.
- [52] Ruangrawee Kitichotkul, Christopher A Metzler, Frank Ong, and Gordon Wetzstein. SUREMap: Predicting Uncertainty in CNN-based Image Reconstruction Using Stein’s Unbiased Risk Estimate. *arXiv preprint arXiv:2010.13214*, 2020.
- [53] Charles Millard, Aaron Hess, Jared Tanner, and Boris Mailhe. Deep Plug-and-Play multi-coil compressed sensing MRI with matched aliasing: the Denoising-P-VDAMP algorithm. In *2022 ISMRM annual meeting*, 2022.
- [54] Singanallur V. Venkatakrishnan, Charles A. Bouman, and Brendt Wohlberg. Plug-and-Play priors for model based reconstruction. In *2013 IEEE Global Conference on Signal and Information Processing*, pages 945–948. IEEE, dec 2013.
- [55] R Ahmad, C A Bouman, G T Buzzard, S Chan, S Liu, E T Reehorst, and P Schniter. Plug-and-Play Methods for Magnetic Resonance Imaging: Using Denoisers for Image Recovery. *IEEE Signal Processing Magazine*, 37(1):105–116, jan 2020.
- [56] Kevin M Johnson, Sean B Fain, Mark L Schiebler, and Scott Nagle. Optimized 3D ultrashort echo time pulmonary MRI. *Magnetic resonance in medicine*, 70(5):1241–1250, nov 2013.
- [57] Paul T. Gurney, Brian A. Hargreaves, and Dwight G. Nishimura. Design and analysis of a practical 3D cones trajectory. *Magnetic Resonance in Medicine*, 55(3):575–582, 2006.
- [58] Saurav K Shastri, Rizwan Ahmad, Christopher A Metzler, and Philip Schniter. Expectation Consistent Plug-and-Play for MRI. *arXiv preprint arXiv:2202.05820*, 2022.